Technical Physics, 2022, Vol. 67, No. 11

13

Electron microscopy of the microstructure of antimony thin films of variable thickness

© V.Yu. Kolosov,[1] A.A. Yushkov,[1] L.M. Veretennikov,[1,2] A.O. Bokuniaeva[1]

[1]Ural Federal University after the first President of Russia B.N. Yeltsin,
Yekaterinburg, Russia
[2]Ural State University of Economics,
620144 Ekaterinburg, Russia
e-mail: yushkov.anton@urfu.ru

Received January 12, 2022
Revised July 26, 2022
Accepted July 27, 2022

Thin Sb films with a thickness gradient deposited in vacuum were investigated by transmission electron microscopy. Microstructures in films with increasing thickness change from amorphous islands of increasing density and size to labyrinthine and continuous films with texturing, which also changes with increasing thickness. Based on the analysis of the patterns of bend extinction contours, a strong internal bending of the crystal lattice, up to 120 deg/μm, and the dependence of the crystallographic orientations in the structures of the film on the thickness were revealed.

Keywords: Antimony, thin films, TEM, crystallography, extinction bend contours.

DOI: 10.21883/TP.2022.11.55181.09-22

Introduction

Antimony is a well-known example of a material in which a very rapid, „explosive“ crystallization phenomenon has been observed in thin films. Antimony is included in materials (e.g. GST — $Ge_2Sb_2Te_5$), that are used to create phase change memory devices (Phase Change Memory — PCRAM, DVD-RW).

The condensation and crystallization of thin antimony films have previously been studied by a number of authors. Thus, the influence of the following parameters on the crystallization rate and critical thickness was investigated: type of substrate [1,2], its temperature [1–3], deposition rate [2,4], relative location of the substrate and substance source [5], and electron irradiation of the substrate [2,6]. Spherulitic crystal growth in [7,8] films has also been investigated. Some characteristic features of the microstructure, including bending contour patterns [9,10], can be seen in the images cited in a number of papers [2,8], but they have not previously been investigated in detail. The presence of numerous bending contours in the case of crystallizing thin films often indicates an internal bending of the crystal lattice, called transrotational [10]. The internal bending is a consequence of a highly non-equilibrium fast-moving amorphous phase−crystalline phase transition. It can serve as a measure of the internal stress, a defect in the structure of the film sample, which can be critical for practical applications.

The objective of this work was to carry out an electron-microskope study of variable-thickness Sb thin films using the bending extinction contour method.

1. Experimental procedure

Thin antimony film samples were obtained by evaporation from the crucible in the VUP-4 unit at a residual pressure of 10^{-3} Pa and deposition onto a mica substrate precoated with a layer of amorphous carbon. The substrate was at room temperature and 10 cm away from the crucible. Spraying was done through a mask with circular holes of 3 mm diameter to create a strong thickness gradient, from 0 to 70 nm per 1 mm. The carbon layer with the antimony film was separated from the substrate on the surface of distilled water and captured with a standard copper grid for electron microscopic examination. The sample was placed in a transmission electron microscope column, and the first images were obtained within one hour of sputtering. Further surveys revealed no change in the samples over time.

The basic investigation was carried out with a JEM-2100 transmission electron microscope at an accelerating voltage of 200 kV in the transmission modes of light and dark field and diffraction. Additionally, X-ray energy dispersive microanalysis — was carried out to assess the mass thickness and composition, and optical microscope imaging — to obtain a general view of the microstructures in the film.

The obtained electron microscopic images were processed mainly in the ImageJ program; electron diffraction patterns were decoded using the CaRIne 3.1 program.

2. Measurements of the internal bending radius of the crystal lattice and the thickness of the crystallites

For the analysis, characteristic areas in different parts of the sample along the thickness gradient — near the phase boundary, in the area of maximum constant thickness of the sample and in the area in between were selected. The ImageJ graphics package was used for processing and measurement. The measurements included an intensity histogram (in the direction perpendicular to the contour at a given point) to accurately locate the positions of intensity minima and maxima at corresponding points in the light-field and dark-field images. For each contour, measurements were taken at several points, depending on the length of the circuit.

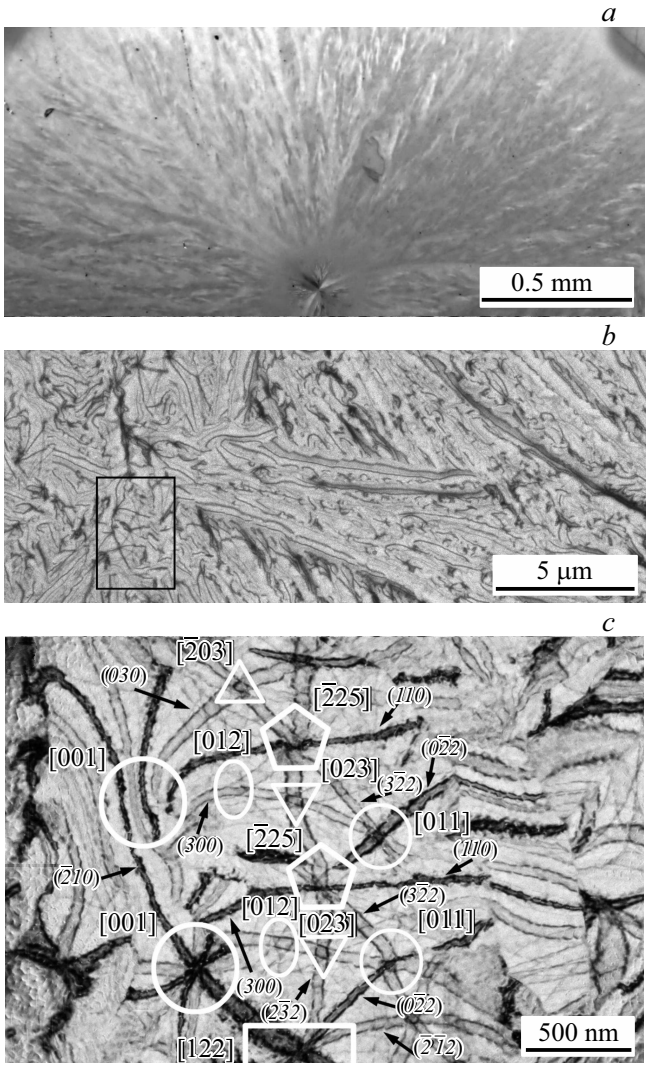

Figure 1. *a* — an image of the crystallization center in the film in polarized light with an optical microscope (3 mm diameter hole trace); *b* — an image of the crystallization center in the film (the area discussed below is highlighted by a rectangle); *c* — crystallization center at higher magnification, with curved contours (indicated by arrows) and zone-axis patterns (highlighted by figures in white).

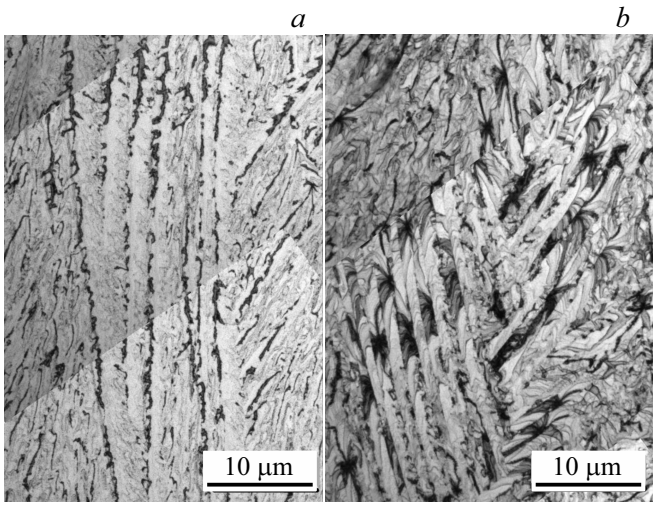

Figure 2. *a* — view (assembly of TEM images) near the phase boundary, extended crystallites with slight curvature in the film plane (azimuthal) can be seen, bending contours can be seen; *b* — view in the area of constant (maximum) film thickness near the crystallization center, packets of crystallites and their separating areas without preferential orientation can be seen, zone-axis patterns of intersecting contours can be seen.

To identify the contours in dark-field mode, the microscope aperture diaphragm highlights a reflex of interest with known crystallographic indices on an electron diffraction pattern of the selected area. The remaining reflexes, including the central, non-diffracted beam, are cut off. As a result, only the selected beam scattered at a certain angle contributes to the image, and only the bending contour corresponding to the selected reflex is illuminated.

Measurements of the inner lattice bending radii in an antimony sample were made by a series of distance measurements between two bright bending contours in the $h\,k\,l$ pair and $\bar{h}\,\bar{k}\,\bar{l}$, taken in the light field mode (Fig. 1, *b, c*, 2) [11]. For such contours (parallel to the bending axis of the crystal or its lattice), from the Wolf–Bragg law of diffraction, according to [11], we can write

$$N = R \cdot 2 \cdot \Theta, \tag{1}$$

where N — the distance between the contours in the pair in the light-field image, R — the bending radius of the crystal [11] (or crystal lattice [12,13] as in our case) around the axis lying in the film plane, Θ — the angle between the $h\,k\,l$ and $\bar{h}\,\bar{k}\,\bar{l}$ planes in reflective position.

Note, that in fact, this formula assumes that the axis of the reflecting planes zone and the normal to the film are parallel to the electron beam, and that the reflecting planes are parallel to the axis of their unfolding on 2Θ. In more general cases, for arbitrary contours, the more complex relations [12] are fulfilled, passing to the considered formula in this simplest case.

Given Wolf–Bragg's law, it is possible to write down the expression for the radius of lattice curvature through the values measured in the images

$$R = 2N/\lambda D, \tag{2}$$

where λ — electron wavelength (0.0025 nm at 200 kV), D — distance between a pair of opposite reflections in the electron diffraction pattern of the selected area.

From the value R, we calculated the internal bending of the lattice per unit length, which we will call the local (internal) specific bending of the lattice, measured in deg/μm.

3. Experimental results and discussion

3.1. Amorphous and crystalline phase boundary

Near the edge of the mask, antimony was deposited as individual amorphous islands whose size and density on the substrate increased along the concentration gradient, until they merged into a cohesive labyrinth structure and then into a continuous film, forming an amorphous-crystalline phase interface (Fig. 3). In some gradient areas, the boundary between amorphous and crystalline phases is clearly outlined, in others, it forms an irregular border with outgrowths of the crystalline phase deep into the labyrinth structure and with isolated amorphous inclusions surrounded by crystalline phase.

3.2. Microstructures in the crystalline phase

Very rare crystallization centers in antimony films are more easily detected by optical microscopy in polarized light (Fig. 1, *a*). One of these centers is shown at a higher magnification in Figure 1, *b* with some of the extinction contours and reflection plane zone axes shown in Figure 1, *c*. The most remarkable crystal (shown as a rectangle in Fig. 1, *b*, and at higher magnification in Fig. 1, *c*) has numerous

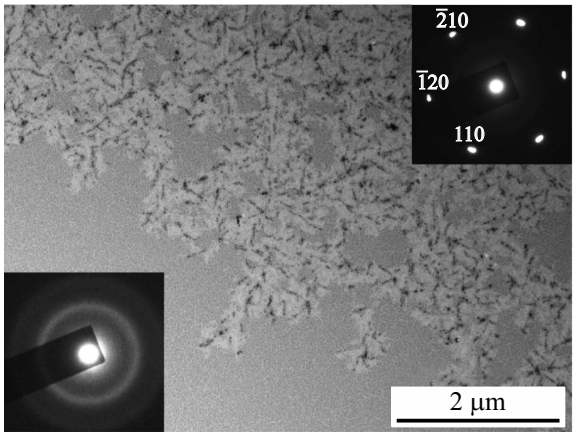

Figure 3. A section of inhomogeneous boundary between crystalline (top) and amorphous (bottom) phases with corresponding electron diffraction patterns.

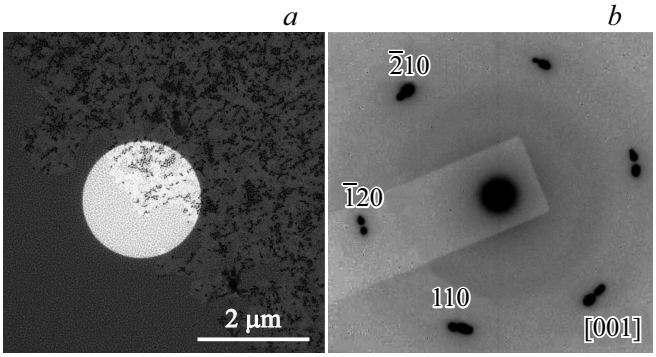

Figure 4. *a* —TEM image of the area of the boundary between the amorphous and crystalline phases at low magnification with a trace of the selector aperture; *b* — electron diffraction pattern of the area highlighted by the aperture in Fig. 4, *a*.

alternating zone-axis patterns indicating noticeable lattice misorientations (as shown below, corresponding to a strong internal bend in the lattice).

Also, according to [11], the film thickness t can be expressed as

$$t = d_{hkl}^2 \cdot N/\lambda k, \tag{3}$$

where d_{hkl} — the interplanar distance, k — the distance between the side intensity maxima in the image (in the dark-field image).

The observed neighboring zone-axis patterns in the crystal indicate a large integral bending of the crystal lattice. We can estimate it by measuring the distance in the image between two identified zone-axis patterns whose angle between the axes of the zones is known. The integral bending of the lattice per unit length in the above crystal takes values from 18 deg/μm between the [023] and [011] zone axes to 36 deg/μm between the [122] and [001] axes, and the local bending — from 13 to 69 deg/μm.

From the center, the crystallization front propagated toward the edges of the sample, forming an almost radially expanding structure (Fig. 1, *a, b*). The most characteristic elements of the microstructure — blocks of weakly disoriented crystallites (which follows from similar zone-axis patterns, see below for details), adjacent to each other. The crystallites are often almost parallel and have a ribbon-like morphology (Fig. 2). They may also have a slight curvature in the sample plane. The crystallites that make up the packets are ribbon-shaped, 100–1000 nm wide and 2–100 μm long. As one moves away from the crystallization center, the length of the crystallites increases (cf. Figs. 2, *a* and *b*), the aspect ratio length/width increases from 10 to 10^3, and the borders become less distinguishable. In areas near the thin edge of the continuous film, such structures are not detected. These areas correspond to the labyrinthine structures of the crystalline and amorphous phase boundaries.

The observed structures can be described as morphological texturing. A large area of the sample cells is filled with

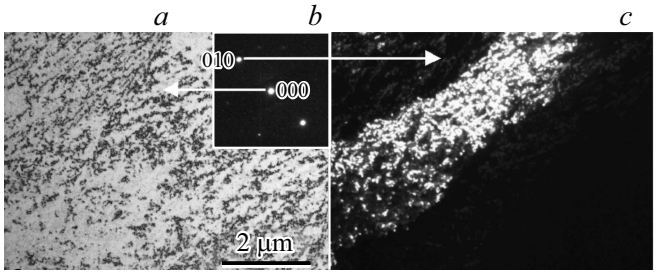

Figure 5. *a* — TEM image of the amorphous and crystalline phase boundary area in the light field mode; *b* — electron diffraction pattern of the area with reflexes marked for imaging; *c* — image of the area in the dark field mode (domains with different lattice orientation are visible).

crystallites forming blocks with co-directional boundaries (Fig. 2). These blocks can clump together in a film of antimony, generally at different angles. The crystallite blocks are adjacent to crystallized areas with no preferential lattice orientation and boundaries (Fig. 2, *b*). Similar zone-axis patterns observed in neighboring crystallites and corresponding electron diffraction patterns indicate close orientations and identical zone axes in them, more often $[\bar{1}111]$. As the film thickness decreases, the areas of the individual packages increase. In this case, in general, the relative tiling area of the film by the interlocking packs does not visually change. In structures adjacent to the crystallization center, the value of the internal bending radius R determined by formula (2) lies in the range of $3.5-5\,\mu$m, this corresponds to a local specific lattice bending of $12-17\,\text{deg}/\mu\text{m}$. The film thickness calculated by formula (3) lies in the range 40–60 nm. For areas near the phase boundary, the bending radius is $1-0.5\,\mu$m (respectively, the local specific bending is $60-120\,\text{deg}/\mu\text{m}$). Thickness measurements by the bending contour method near the amorphous phase–crystallized film boundary were not carried out since no secondary contour maxima are detected in this area in the dark field, but by direct observation (bends, film breaks) the thickness was estimated as 10–15 nm.

The change in the average film thickness (thickness gradient) in the sample can be clearly seen directly on the screen of a transmission electron microscope by the decrease in the overall brightness of the image as one moves deeper into the sample: as the thickness increases, the transparency of the sample for the electron beam decreases and, consequently, the intensity of the image decreases. There is also a gradual increase in antimony content on the sample plane, as we move from islands to the thickest areas (including the passage of the boundary of amorphous and crystalline phases and the zone of solid film formation due to growth in size, number and cohesion of islands Sb).

3.3. Crystallographic orientations in Sb film

In areas of continuous antimony film, it shows extended bending contours, often intersecting with the formation of zone-axis patterns. In structures near the crystallization center (packages of crystallites and disordered areas), the orientation of the zone axis $[\bar{1}11]$ prevails. With approach to the boundary of the amorphous and crystalline phases, the [001] orientation prevails; as a rule, only this orientation is found in the area of labyrinthine boundary structures.

It was found that near the phase boundary in the film, the lattice azimuthal misorientations are small, on the order of a few degrees, and rare within one cell of the subject grid (at a distance of tens of μm) (Fig. 4).

There are disorientations of the zone axis from the position perpendicular to the film, revealed as orientation domains in the dark field (Fig. 5).

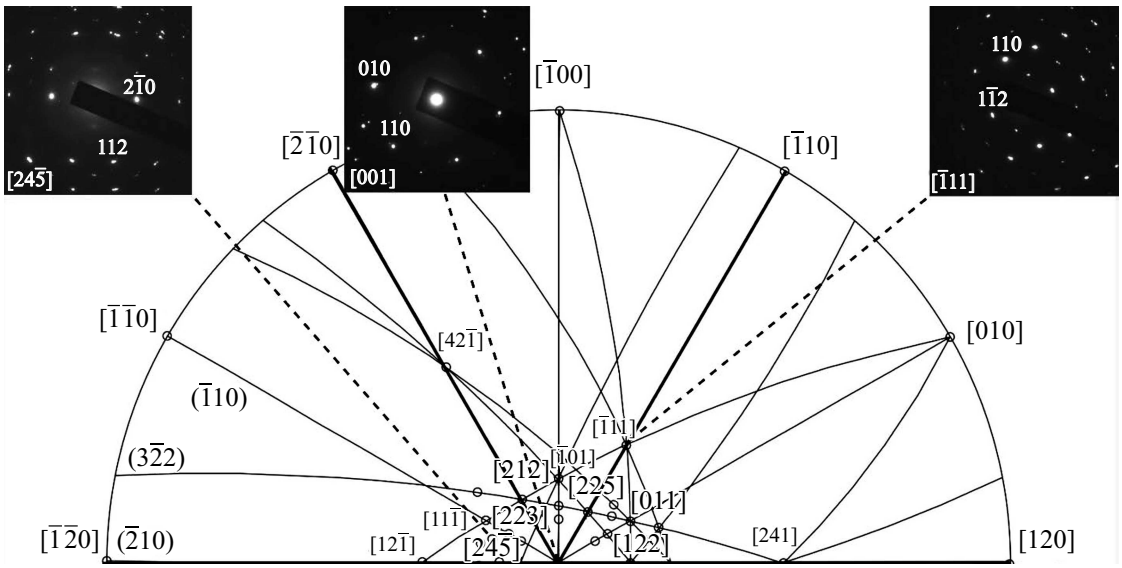

Figure 6. Stereographic projection of some crystallographic planes (corresponding to pairs of bright contours on the microphotographs) and zone axes revealed on electron diffraction patterns (marked with a black dot, including [001] in the center).

For areas close to the crystallization center, a stereographic projection was constructed with some bending contours and prevailing zone-axis patterns with the [001] zone axis in the center (Fig. 6) corresponding to a denser packing of perpendicular crystallographic planes.

Conclusion

Rare crystallization centers in the film areas with the greatest thickness were identified. Crystallization extends into the area of less thickness, up to the boundary of the labyrinthine structure formed by cohesive islands of condensed matter.

According to the bending contour measurements, the antimony sample showed significant internal bending of the crystal lattice, up to 120 deg/μm, its predominantly elastic curvature around the axis lying in the film plane, corresponding to transrotational microcrystals [10]. These values are large, but are within the limits possible for elastic deformation of thin crystals. This feature has been previously revealed for thin films of various materials, such as selenium and its compounds 13, iron oxide 14, and some practically important materials studied in other groups [15–18].

It was shown that the bending radius (around the axis lying in the sample plane) decreased by an order of magnitude with decreasing crystal film thickness, from ~ 5 to $\sim 0.5\,\mu$m. The dependence of the bending radius on film thickness has been previously observed for other materials.

The samples reveal texturing in the form of packets of more or less elongated crystallites, usually with close crystallographic orientations, resulting from the spread of crystallization from rare crystallization centers. As the thickness of the crystal film decreases, the aspect ratio of length to width for crystallites changes greatly. It was determined by comparing images with magnification on the order of $\times 5000$ — to determine crystal width and with magnification on the order of $\times 300 - \times 500$ — to estimate length. It grows from 10 to about 10^3.

As a result of decoding the majority of electron diffraction patterns, the zone axis orientation was found to be the most characteristic of labyrinth structures and areas of small thickness of the continuous film [001]. The $[\bar{1}11]$ orientation is more typical in the most-thick areas, near the crystallization centers, in packets of parallel crystallites; in disordered" crystallized areas between packets, the [001] and some others, including [101], $[\bar{2}25]$ orientations are also detected.

Funding

This work was supported by grants from the Russian Foundation for Basic Research 19-32-90255 and 20-02-00906.

Conflict of interest

The authors declare that they have no conflict of interest.

References

[1] M.H.B. Stiddard. J. Mater. Sci. Lett., **4**, 1157 (1985).
[2] K.L. Chaudhary, R. Kumar, A.K. Chopra. Defence Science J., **50** (4), 411 (2000).
[3] M. Hashimoto, K. Kambe. Thin Solid Films, **94**, 185 (1982).
[4] N. Kaiser. Phys. Stat. Sol. A, **81** (99), 99 (1984).
[5] M. Hashimoto. Thin Solid Films, **115**, 309 (1984).
[6] M. Hashimoto. Thin Solid Films, **113**, 25 (1984).
[7] H. Muller. Phys. Stat. Sol. A, **66** (199), 199 (1981).
[8] H. Muller. Phys. Stat. Sol. A, **70** (249), 249 (1982).
[9] P. Hirsch. *Electron microscopy of thin crystals* (Mir, M., 1968)
[10] V.Yu. Kolosov, A.R. Thölén. Acta Mater., **48**, 1829 (2000). https://doi.org/10.1016/S1359-6454(99)00471-1
[11] P. Delavignette, R.W. Vook. Phys. Stat. Sol., **3**, 648 (1963).
[12] I.E. Bolotov, V.Yu. Kolosov. Phys. Stat. Sol. A, **69**, 85 (1982).
[13] V.Y. Kolosov, L.M. Veretennikov. Poverkhnost', **2**, 70 (2000).
[14] V.Yu. Kolosov, A.R. Tholen. Nanostructured Materials, **9**, 323 (1997).
[15] B.J. Kooi, J.T.M. De Hosson. J. App. Phys., **95**, 4714 (2004).
[16] P. La Fata, F. Torrisi, S. Lombardo, G. Nicotra, R. Puglisi, E. Rimini. J. App. Phys., **105** (8), 123 (2009).
[17] V. Longo, M.A. Verheijen, F. Roozeboom, W.M.M. Kessels. ECS J. Sol. St. Sci. Tech., **2** (5), 120 (2013).
[18] A. Alberti, C. Bongiorno, B. Cafra, G. Mannino, E. Rimini, T. Metzger, C. Mocuta, T. Kammler, T. Feudel. Acta Cryst. B, **61**, 486 (2005).